



# Austenite reversion suppression with deep cryogenic treatment: A novel pathway towards 3rd generation advanced high-strength steels

Patricia Jovičević-Klug<sup>a,b,1,\*</sup>, Matic Jovičević-Klug<sup>b,1</sup>, Lars Thormählen<sup>c</sup>, Jeffrey McCord<sup>c</sup>, Michael Rohwerder<sup>b</sup>, Matjaž Godec<sup>a</sup>, Bojan Podgornik<sup>a</sup>

<sup>a</sup> Institute of Metals and Technology, Lepi pot 11, 1000, Ljubljana, Slovenia

<sup>b</sup> Max-Planck Institute for Iron Research, Max-Planck-Str. 1, 40237, Düsseldorf, Germany

<sup>c</sup> Institute for Materials Science, Kiel University, Kaiserstraße 2, 24143, Kiel, Germany

## ARTICLE INFO

### Keywords:

Martensitic stainless steel  
Deep cryogenic treatment  
Microstructure  
Mechanical properties  
Microstructural transformations

## ABSTRACT

This study investigates the impact of deep cryogenic treatment (DCT) on microstructure and properties of a martensitic stainless steel AISI 431. The reasonably simplistic microstructure tailoring with DCT delivers a novel pathway towards advanced 3rd generation high-strength steels (AHSS), whilst utilizing existing alloys and chemistry. The resulting microstructural changes deliver improved strength and hardness of the material, whilst still sustaining good elongation properties. DCT reduces the material's toughness but improves its deformation resistance and wear resistance. The study reveals that DCT modifies the microstructural evolution during tempering. During the conventional treatment, AISI 431 develops austenite reversion transformation (ART), which allows the high strength and elongation capabilities formed with transformation-induced plasticity (TRIP). In contrast, DCT progresses the microstructure even further by retransforming the reverted austenite formed through ART into tertiary  $\alpha$ -martensite,  $\epsilon$ -martensite and carbides that increase the strength and deformation behavior of AISI 431. The novel microstructural modification that we have entitled cryogenic austenite retransformation (CAR), is both experimentally and theoretically assessed. The underlying transformation mechanisms of CAR and individual stages of DCT were evaluated with ex-situ electron backscatter diffraction and transmission electron microscopy. The impact of DCT on the modified transformation capabilities of AISI 431 is discussed in relation to possible implementation in automotive industry as a universally applicable treatment procedure.

## 1. Introduction

Deep cryogenic treatment (DCT) has emerged as a treatment procedure that can influence the microstructural properties of metals and alloys from the nano-scale to the macro-scale [1–3]. The microstructure is modified by exposing the treated material to cryogenic temperatures below  $-150\text{ }^{\circ}\text{C}$  or even lower, which inhibit changes in the stress state of the material and thereby induce intricate changes to the dislocation network and local equilibrium energy potentials of solute atoms [1,4,5]. Such modifications result in phase reformation as well as advanced precipitation and secondary phase formation [1,4,6]. The effects range from the austenite to martensite transformation through adiffusional lattice shearing, which is characteristic for ferrous alloys, to promoted

finer precipitation of carbides and precipitates that has been reported for both ferrous and non-ferrous alloys [7–9]. The nature and sequence of precipitation can also be modified, resulting to new microstructural designs and states that also influence the final mechanical and surface properties. For example, DCT has been reported to improve hardness [10–13], strength [10,14–17], toughness as well as corrosion and wear resistance [3,18–24]. However, despite these many potential beneficial modifications through DCT, an important knowledge gap exists regarding the effect of DCT on high-alloyed and high-strength steels. Additionally, the effect of DCT on specific microstructural mechanisms such as transformation-induced plasticity (TRIP), twinning induced plasticity (TWIP) and austenite reversion transformation (ART) [25] is not well understood. These mechanisms play a crucial role in the

\* Corresponding author. MPIE, Max-Planck-Str. 1, 40237, Dusseldorf, Germany.

E-mail addresses: [patricia.jovicvicklug@imt.si](mailto:patricia.jovicvicklug@imt.si), [p.jovicvicklug@mpie.de](mailto:p.jovicvicklug@mpie.de) (P. Jovičević-Klug), [m.jovicvicklug@mpie.de](mailto:m.jovicvicklug@mpie.de) (M. Jovičević-Klug), [lath@tf.uni-kiel.de](mailto:lath@tf.uni-kiel.de) (L. Thormählen), [jmc@tf.uni-kiel.de](mailto:jmc@tf.uni-kiel.de) (J. McCord), [m.rohwerder@mpie.de](mailto:m.rohwerder@mpie.de) (M. Rohwerder), [matjaz.godec@imt.si](mailto:matjaz.godec@imt.si) (M. Godec), [bojan.podgornik@imt.si](mailto:bojan.podgornik@imt.si) (B. Podgornik).

<sup>1</sup> These authors contributed equally.

development of novel high-strength steels (AHSSs) that are exceedingly needed for the development of advanced applications in the automotive, aerospace, construction and energy industries [26,27]. Furthermore, the direct relation between the microstructure and mechanical properties in connection to the previous mechanisms influenced by DCT is completely missing, creating a considerable knowledge gap on the impact of DCT for such ferrous alloys.

AHSSs are classified into three generations based solely on their ductility and strength [26,27] (Fig. 1a): 1st generation AHSSs are primarily based on the ferrite phase and its transformations into other phases (bainite, martensite, retained austenite, dual phase) [26–28]. The 2nd generation AHSSs is based on the utilization of austenite-based matrix and its change with TWIP and shear band strengthening [26–28]. However, 2nd generation AHSSs has high production cost, which limits its production and application in industry [28]. The 3rd generation is the latest generation of AHSSs that aims to achieve the high strength and elongation of the 2nd generation and the ease of production and low cost of the 1st generation. In addition, with great concern about emissions from the automotive industry and its production, automakers are intensively searching for new and improved AHSSs and engineering techniques that would minimize the industry's environmental footprint, which is the additional goal of the 3rd generation AHSSs [26,27]. The main challenge in developing the next generation of AHSSs is the general trade-off between their strength and ductility resulting from microstructural manipulation and alloy modification [26,27]. The aforementioned mechanisms and the development of complex multi-phase steels (such as austenite-martensite duplex steels) can partially overcome the trade-off, but at the expense of complex processing and limited microstructural stability in high-temperature, corrosive [29] and wear environments [30]. In this regard, novel and simpler approaches are required to advance the development of AHSS while maintaining their economic viability and versatility for a wide range of applications [26,27]. These are also the main reasons for the strong support and emergence of research on potential 3rd generation AHSS (see Fig. 1a) within the last 5 years [26–28], which offer unique strength-ductility properties engineered through multi-phase microstructure, thermo-mechanical processing, novel treatment processes and selective alloying [26,27].

This work provides the first insight into the highly modified microstructure of a martensitic stainless steel, AISI 431, which with additional DCT application has the potential to be used as a new candidate for 3rd generation AHSS. In addition, our work provides the first detailed understanding of the DCT mechanism and its potential application for successful microstructural modification of selected steels and steels with similar chemical composition and microstructural base. This study shows that DCT induces a unique microstructural mechanism, which we have discovered and termed Cryogenic Austenite Retransformation (CAR). This phenomenon develops a special partitioning of the reverted austenite into multiple phases that would not normally occur for AISI 431 under the selected conventional heat treatment (CHT) procedure. With the new explored mechanism, we pave the road towards a novel

modification of ferrous alloys with DCT that can deliver new combinations of microstructure and properties. Moreover, this work also evaluates the changes induced by DCT on the final properties due to the initiation of the novel mechanism, which provides high strength and good elongation properties well within the required range of 3rd generation AHSSs (see Fig. 1a). This is achieved through a systematic study of the microstructure and mechanical properties (hardness, fracture and impact toughness, work hardening, compressive and tensile strength) as well as fatigue and wear properties and their correlation, from which we provide an in-depth understanding of the effect of DCT on AISI 431. In addition, we also compare the effect of different heat treatment parameters on the microstructure and property development of DCT material, from which we derive the possibility of using DCT under different heat treatment conditions and processes. Finally, we demonstrate the feasibility of utilizing DCT as a process for segmental tailoring of the material to develop intricate variation of material properties within the same workpiece with a single heat treatment process, which would expand the utilization and applicability of steels for various demanding applications.

## 2. Experimental procedure

### 2.1. Material and heat treatment

AISI 431 steel (also known as EN X17CrNi16-2 and 1.4057), a martensitic stainless steel (MSS), was selected for this study. The material was supplied by the company MDM, Slovenia, in the form of rolled, peeled and soft annealed bars of  $\varnothing$  20 mm. The chemical composition of the steel material, measured by ICP-OES Agilent 720, is given in Table 1.

The heat treatment process for selected steels is shown schematically in Fig. 1. The exact parameters of each stage are given in the accompanying boxes within Fig. 1.

The heat treatment of the specimens is performed first with austenitization at 1050 °C for 30 min. All specimens were heat treated in a horizontal vacuum furnace Ipsen VTTC324-R, which was also used for subsequent tempering of the specimens. Quenching from austenitizing temperature to room temperature was performed in N<sub>2</sub> gas at 5 bar pressure to achieve a predominantly martensitic matrix of the material. The specimens were then divided into two groups, a control group of conventionally heat treated (CHT) specimens and a test group of DCT specimens, denoted as CHT1 and DCT1, respectively. The CHT specimens were immediately annealed using the specified annealing procedure shown in Fig. 1. In contrast, the DCT group was subjected to a controlled deep cryogenic environment of −196 °C by gradual immersion in liquid nitrogen (LN<sub>2</sub>) for 24 h (cooling and warming rate of approximately 10 °C min<sup>−1</sup>) prior to annealing. After reaching room temperature, the DCT specimens were finalized by the same tempering procedure as the CHT counterpart group in order to have comparability between CHT and DCT specimens and their properties. The treatment temperatures and time parameters for austenitizing and tempering were

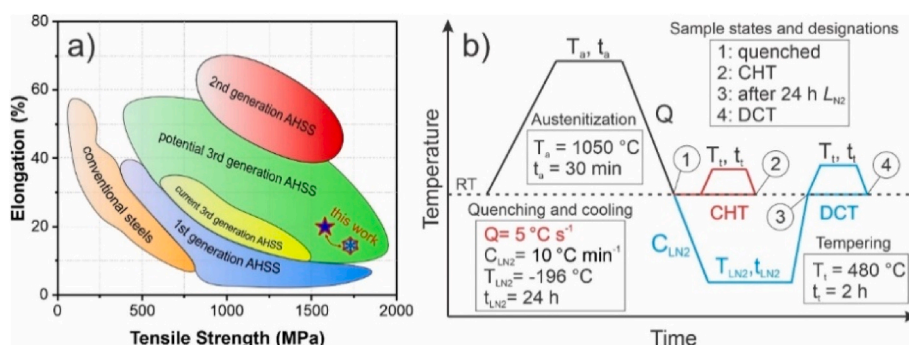


**Fig. 1.** (a) Simplified global formability diagram showing the placement of the newly proposed processing of AISI 431 steel grade as a potential 3rd generation AHSS (marked with star and snowflake). (b) Scheme of set heat treatments with selected heat treatment temperatures ( $T_a$  and  $T_t$ ) and treatment times ( $t_a$  and  $t_t$ ) and cooling rates ( $Q$  and  $C_{LN_2}$ ), where CHT (red line) are conventionally heat-treated subgroups and DCT (blue line) are deep cryogenic heat-treated subgroups. (For interpretation of the references to color in this figure legend, the reader is referred to the Web version of this article.)

**Table 1**  
Chemical composition of selected steel AISI 431 in mass percent (wt.%).

steel grade (AISI)	C	Mn	S	Cr	Si	Ni	Mo	Fe
431 martensitic stainless steel	0.17	0.83	0.017	15.22	0.29	1.50	0.11	base

chosen to obtain the highest tensile strength values of CHT AISI 431. The other parameters related to DCT and quenching were chosen based on previous experience related to DCT research.

In order to determine the effect of heat treatment temperatures ( $T_a$  and  $T_i$ ) on the effectiveness of DCT and the resulting properties of the selected material, another set of specimens was prepared using the same procedures and processing parameters as described above with different heat treatment temperatures of  $T_a = 980$  °C and  $T_i = 600$  °C. These temperatures represent the most common heat treatment procedure for the AISI 431 grade, providing good combination of strength and toughness [31,32]. The corresponding final states of the material after each treatment of the second set will be designated as CHT2 (conventionally heat treated 2) and DCT2 (deep cryogenically heat treated 2).

## 2.2. Methods

### 2.2.1. Microscopy and phase analysis

The final and intermediate states of the treated samples (positions marked from 1 to 4 in Fig. 1b) were prepared metallographically by grinding and polishing with silica paper and finished with colloidal silica suspension. The microstructure of the specimens was examined by optical microscopy (OM) using Zeiss Axio Imager.Z2m with Zen software (Carl Zeiss AG, Germany) and scanning electron microscopy (SEM) using Jeol JSM-6500F. For microstructural examination, the specimens were etched with 10% ferric chloride solution to reveal mainly the presence of austenite, as well as with Kalling's etchant to provide more insight into the remaining microstructural features such as precipitated carbides and martensite grains, following the guidelines for preparation of DCT specimens [33]. For microscopic phase analysis, electron backscatter diffraction (EBSD) was performed (Zeiss CrossBeam 550 Edax Hikari Super plus camera) and the data are presented as inverse pole figures with color coding for orientation designation based on primary crystallographic orientations. In addition, EDX (energy dispersive X-ray spectroscopy) was used to analyze the chemical composition of the precipitates and matrix. Transmission electron microscopy (TEM) with a JEOL JEM-2100 HR TEM microscope at 200 kV accelerating voltage was used for nanoscopic examination of the samples. The corresponding local phase determination was performed by selected area electron diffraction (SAED). The SAED data were analyzed using SingleCrystal phase identification software. Local EDX was also performed to assess the local chemical composition of individual phases within the samples.

### 2.2.2. Vibrating sample magnetometer

To determine the fraction of non-magnetic phases in the treated samples, cylindrical samples 5 mm in diameter and 2.5 mm high were measured using a Lake Shore Cryotronics Model 7404 Vibrating Sample Magnetometer (VSM, OH-USA). To determine the bulk magnetization, the VSM was calibrated with a Lake Shore nickel standard, model 730908, which has a magnetic moment of 6.92 mA/m<sup>2</sup> at room temperature and an applied magnetic field of 500 mT. The samples were mounted with their tops on the sample holder and the samples were measured along the lateral surface of the cylinder. To achieve full magnetic saturation of the samples, measurements were performed in a field range from -1.7 T to 1.7 T with different increments between 60 mT and 8 mT.

### 2.2.3. Mechanical and fatigue testing

#### 2.2.3.1. Hardness.

Hardness was measured under room conditions

(21 °C and 50% humidity) using the Rockwell C method for each heat treatment group. Multiple measurements were performed on several specimens (at least 6) and the mean and standard deviation were calculated. For the hardness measurement performed on cylindrical specimens, the curvature correction was applied according to the SIST EN ISO 6508-1 (2016) standard.

**2.2.3.2. Impact and fracture toughness.** Impact toughness was measured at room conditions (21 °C and 50% humidity) with the Charpy impact test according to the international standard SIST EN ISO 148-1:2017, using standard Charpy V-notch specimens (at least 3 replicates) and a 300 J pendulum. Fracture toughness was measured at room conditions (21 °C and 50% humidity) on CNPTB specimens [34] that were fatigue-precracked prior to heat treatment by subjecting them to single-point cyclic loading for several minutes to produce a pre-crack region approximately 0.5 mm wide. After the selected heat treatment, the specimens (at least 6) were mounted in the INSTRON 1255 500 kN universal tensile testing machine and axially loaded at a displacement rate of 0.0167 mm/s to failure.

**2.2.3.3. Compressive strength and strain-hardening exponent.** The tests were performed under room conditions (21 °C and 50% humidity) using the INSTRON 1255 (Instron, MA-USA) universal testing machine at a constant compression rate of 2 mm/min until maximum plastic deformation or sudden fracture of the specimen occurred. Compressive strength was measured according to ASTM E9-19 using a minimum of 3 cylindrical specimens with dimensions of 10 × 10 × 1 mm. From the compression test, the strain hardening exponent was determined from the true stress-true strain curve (from the onset of plastic deformation to the maximum compressive stress).

**2.2.3.4. Tensile strength and elongation.** The tensile strength and elongation of the steel were measured under room conditions (21 °C and 50% humidity) using INSTRON 8802 (Instron, MA-USA) and the SIST EN ISO 6892-1 standard. Testing was performed on a minimum of 3 B20 cylindrical specimens measuring 92 × 10 mm.

**2.2.3.5. Fatigue.** Fatigue resistance was tested at ambient conditions (21 °C and 50% humidity) under dynamic loading in bending mode using a Cracktronic Rumul (Rumul, Switzerland) resonant fatigue testing machine with an operating frequency of approximately 170 Hz. Fatigue tests were performed on standard Charpy V-notched specimens (10 × 10 × 55 mm) using constant amplitude bending stress between 250 MPa and 400 MPa, stress ratio R of 0.1, and a sinusoidal waveform. The failure criterion for the specimens was set as a decrease in inherent oscillation of more than 3%, with fatigue cracks occurring to a depth of up to 3 mm. The data were then fitted using the Pearl-String method and plotted as a linear function.

### 2.2.4. Wear testing

Abrasive wear resistance and coefficient of friction were determined under dry reciprocating sliding conditions (room conditions, 21 °C and 50% humidity) using a ball-on-flat contact configuration with a stroke length of 4 mm, using Al<sub>2</sub>O<sub>3</sub> (1750 HV) as the counterbody to promote abrasive sliding wear. Four different loading conditions were applied (see Table 2), using two loads of 102 N and 30 N and two sliding velocities of 0.12 m/s (at 15 Hz) and 0.01 m/s (at 1 Hz), resulting in a total distance of 200 m and 60 m, respectively. The wear volume was measured using a 3D confocal focus variation microscope - Alicona

**Table 2**  
Sliding conditions.

Sliding condition	Speed (m/s)	Contact pressure (GPa)
Condition 1	0.01	30
Condition 2	0.01	102
Condition 3	0.12	30
Condition 4	0.12	102

InfiniteFocus (Alicona, Austria), from which the wear rate was calculated. The wear scars were also examined using a scanning electron microscope (SEM), JSM-6500F (Jeol, Japan), to identify/confirm wear-related failures and defects. The coefficient of friction (COF) was continuously recorded during sliding and its average value was evaluated from the steady state condition, which was set as 800–1666 s for sliding speed of 0.12 m/s and 500–7500 s for sliding speed of 0.01 m/s.

### 3. Results and discussion

#### 3.1. DCT effect on microstructure

The comparison of the final states of AISI 431 after CHT1 and DCT1 reveals a surprisingly different microstructure (compare Fig. 2a with 2b). In particular, the amount of austenite content (best resolved as a bright phase in the dark field mode of OM Fig. 2a–b) is shown to be significantly higher for the CHT1 sample compared to the DCT1 counterpart. The austenite is randomly distributed throughout the CHT1 sample as  $\mu\text{m}$ -sized particles located within the martensitic matrix. Closer inspection with the SEM (Fig. 2c–d) reveals a different remodeling of the matrix, which is more segmented and heterogeneous in the DCT case than in the CHT1 case. The DCT1 sample shows a different contrast of the martensite matrix with significantly larger darker patches of martensite (see marked regions in Fig. 2d), indicating a different state of martensite compared to that of CHT1. By specifically etching the material with Kaling's etchant, it is found that the martensite matrix is not only composed of the typical  $\alpha$ -martensite, but also of individual regions of  $\varepsilon$ -martensite after both heat treatment schemes (Fig. 2e–f). However, for the DCT1 case, the  $\varepsilon$ -martensite structures are larger and form in greater amounts compared to those found in the CHT1 samples. In addition to the increased  $\varepsilon$ -martensite formation, the increased precipitation of nanoscale particles is also induced. As can be seen from the comparison of Fig. 2g and f, the DCT1 sample shows a richer formation of precipitates within individual martensitic laths as well as a thicker formation of carbides at the grain boundaries. Regardless, both CHT1 and DCT1 samples show the formation of the carbides with an elongated morphology in the bulk of the martensitic laths that appears to follow

the crystal orientations of the martensitic laths.

Further analysis with EBSD (Fig. 3) additionally confirms the significantly reduced formation of austenite for the DCT1 treated sample compared to the CHT1 counterpart. The additional analysis of the quenched state (Fig. 3a) and the state after 24 h immersion in  $\text{LN}_2$  (Fig. 3c) further elucidate that the austenite in the CHT1 sample is formed due to the tempering process and that the retained austenite after quenching is reduced by immersion in  $\text{LN}_2$ . This confirms the proposed theory of (ART), which originates from the destabilized martensitic structure during exposure to elevated temperatures [35], and illustrates that DCT causes a significant change in the development of the microstructure during the tempering process.

In addition, EBSD shows the much denser formation of precipitates and  $\varepsilon$ -martensite with DCT, suggesting that the reversion process is hindered either by reformation of the  $\alpha$ -martensite matrix to  $\varepsilon$ -martensite or by conversion of austenite to  $\varepsilon$ -martensite, both of which lead to additional formation of carbides. This is also a reasonable assumption since DCT1 samples show agglomerated formation of  $\varepsilon$ -martensite and carbides in a similar shape and size range as the austenite in the CHT1 samples (compare Fig. 3b–d). In addition, the EBSD maps show that the martensitic matrix is mostly segmented at the interfaces of larger martensitic lamellae for the DCT1 samples (Fig. 3d), whereas the segmentation of the martensite does not occur for the CHT1 samples (Fig. 3b), suggesting that the segmentations result from a microstructural sub-process that occurs during the tempering process in the DCT case.

TEM examination of the samples (Fig. 4) confirms the presence of  $\varepsilon$ -martensite as well as  $\text{M}_{23}\text{C}_6$  carbides in both CHT1 and DCT1 samples. As observed from the SEM study, the carbides for the DCT1 samples are mainly formed in close proximity to the  $\varepsilon$ -martensite lamellae, whereas for the CHT1 case the carbides are preferentially formed at the boundaries of the  $\alpha$ -martensite matrix and regions close to the austenite phase. For both samples, austenite is found interspersed between martensitic laths of both martensite types (Fig. 4a and e), which correlates well with the proposed formation from the  $\alpha$ -martensite. Interestingly, the carbides for the DCT case show an additional subtype associated by its crystallography with the  $\text{M}_3\text{C}$  carbides (see Fig. 4d), which are formed within or close to the boundary of  $\varepsilon$ -martensite. Such formations indicate the possible influence of  $\varepsilon$ -martensite formation on the formation of new carbides that follow the dealloying effect caused by the more tightly bound  $\varepsilon$ -martensite compared to  $\alpha$ -martensite [36,37].

In contrast to the first group of samples (CHT1 and DCT1), the second group (CHT2 and DCT2) with different heat treatment temperatures generally shows a negligible change in microstructure with DCT. The resulting micrographs, shown in Fig. 5, show a more segmented matrix

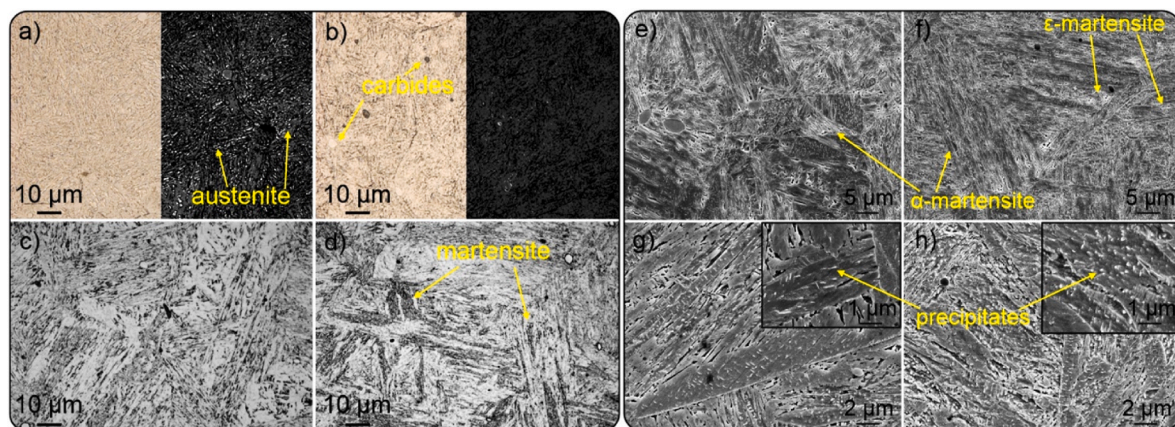


**Fig. 2.** Optical micrographs of (a) conventionally heat treated (CHT1) and (b) deep cryogenic treated (DCT1) samples etched with 10% ferric chloride solution obtained in bright-field (left) and dark-field mode (right). (c–d) optical micrographs of (c) CHT1 and (d) DCT1 samples etched with Kaling's etchant. (e–h) Scanning electron micrographs of (e, g) CHT1 and (f, h) DCT1 samples etched with Kaling's etchant.

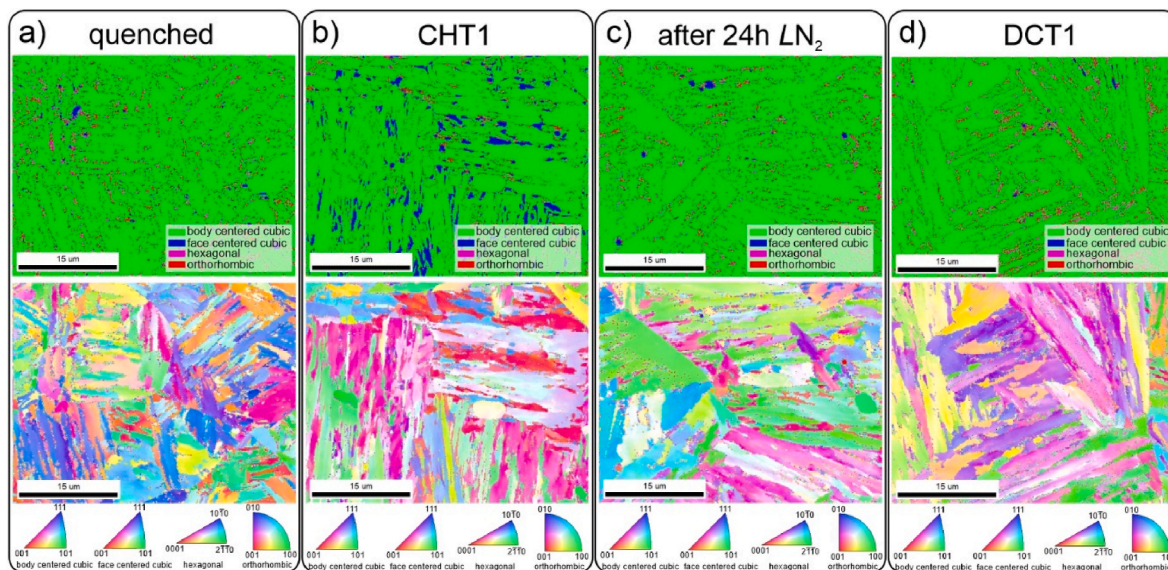


**Fig. 3.** Electron backscatter diffraction maps and complementary inverse pole figures of (a) quenched state of the samples, (b) conventionally heat treated (CHT1) samples, (c) samples after immersion in liquid nitrogen ( $LN_2$ ) without tempering and (d) deep cryogenic treated (DCT1) samples.

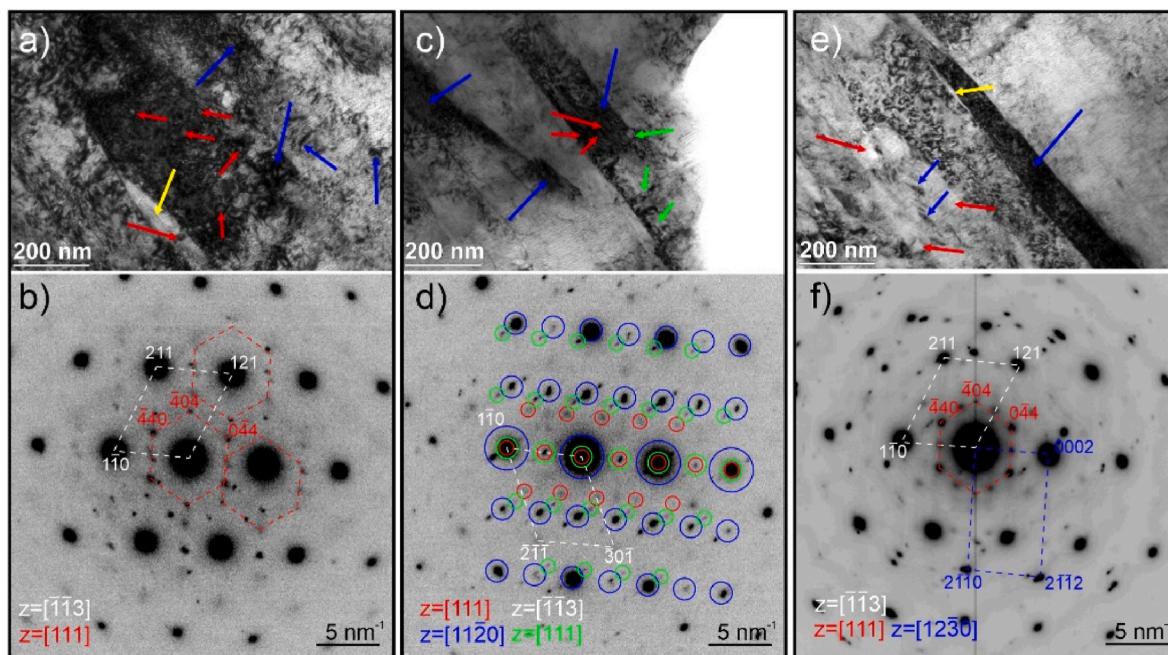


**Fig. 4.** Transmission electron microscopy images of (a) conventionally heat-treated (CHT1) and (b, c) deep cryogenic treated (DCT1) samples. The corresponding selected area electron diffraction patterns are shown in (b), (d) and (f). The different colored arrows and basic unit cells correspond to the different phases found in the samples.  $\alpha$ -martensite is marked with white,  $M_{23}C_6$  carbides with red,  $M_3C$  carbides with green,  $\epsilon$ -martensite with blue and austenite with yellow. (For interpretation of the references to color in this figure legend, the reader is referred to the Web version of this article.)

(Fig. 5a–b) and a denser population of carbides, particularly at the grain boundaries of martensite and former austenite grain boundaries for the second group of samples compared to the first one. No austenite was detected by EBSD (see Supplementary Material S1), indicating a lack of ART activation in such a heat treatment process, probably due to the higher tempering temperature. In addition, both samples show the formation of much larger carbides and a stronger carbide enrichment at grain boundaries compared to the previous heat treatment group. Due to the larger size, local EDS maps (see Supplementary Material S1) confirm that the larger carbides are Cr enriched, which implies that the larger carbides are of the Cr-rich  $M_{23}C_6$  type, determined also from previous

XRD analysis of such material and local EBSD identification (see Supplementary Material S1). Nevertheless, the DCT2 sample still showed a higher carbide density compared to its CHT2 counterpart (compare Fig. 5c to d). This is further confirmed by EBSD (see Supplementary Material S1). Due to the much finer structure of the martensitic matrix and the local features identified as carbides and  $\epsilon$ -martensite, the absence of austenite cannot be simply deduced as the austenite could also be segmented and present as nanoscopic phases between the carbide and martensite lamellae. To further confirm the absence of austenite in these samples, magnetic characterization using VSM was performed.

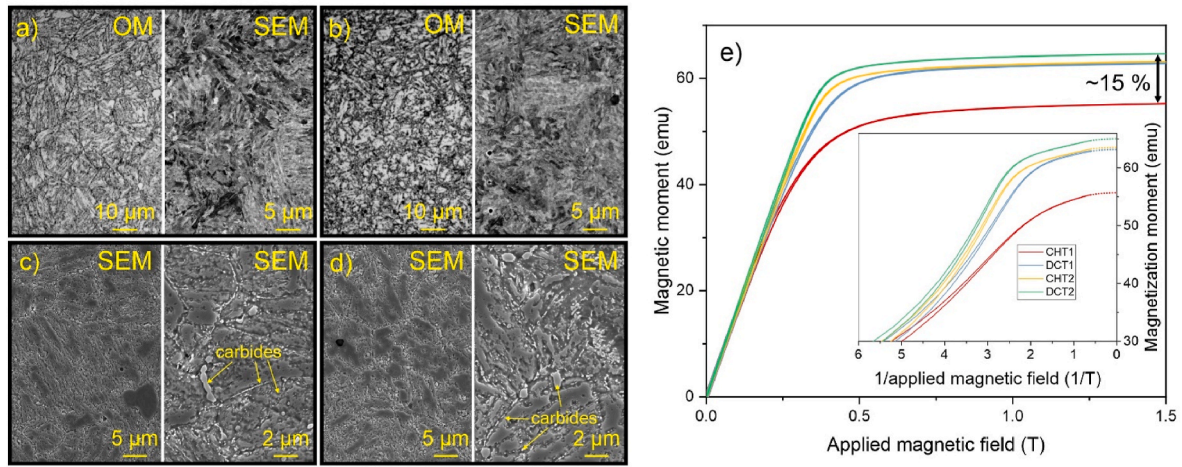


**Fig. 5.** Optical micrographs (OM) and scanning electron micrographs (SEM) of (a) conventionally heat treated (CHT2) and (b) deep cryogenic treated (DCT2) samples etched with 10% ferric chloride solution. (c–d) Scanning electron micrographs of (c) CHT2 and (d) DCT2 samples etched with Kalling’s etchant. (e) Magnetization response of all 4 samples measured with vibrating sample magnetometry. The inset shows the data plotted with 1/applied field which allows extrapolation of the maximum magnetization moment (extrapolations represented by the dashed curves).

Looking at the magnetic response of the material to large external magnetic fields, the magnetic saturation can be related to the fraction of non-magnetic phases present in the different samples, since austenite is non-magnetic while the matrix and carbides are ferromagnetic [38,39]. The VSM data in Fig. 5e show that only the CHT sample has a significantly lower magnetic saturation compared to the other samples. Comparing the phase fractions determined from the XRD measurements [32], the saturation magnetization closely follows the austenite phase fraction, with the difference between the CHT1 and DCT2 samples being approximately 15% (assuming no austenite phase is present in DCT2 based on microstructural observations). By plotting the data with

1/applied field (see inset of Fig. 5e), the magnetic saturation can be more accurately determined and extrapolated as the applied fields go to infinity (see dashed curves). The maximum difference between CHT and DCT2 is then found to be 14.4%, which correlates well with the austenite phase fraction determined by XRD [32]. VSM also confirms that DCT allows further transformation of austenite to martensite even in the second heat treatment, i.e. DCT2 allows complete removal of austenite from the studied steel grade. It also confirms that DCT still modifies the microstructure to some extent in the second heat treatment group, although less dramatically than in the first heat treatment group.

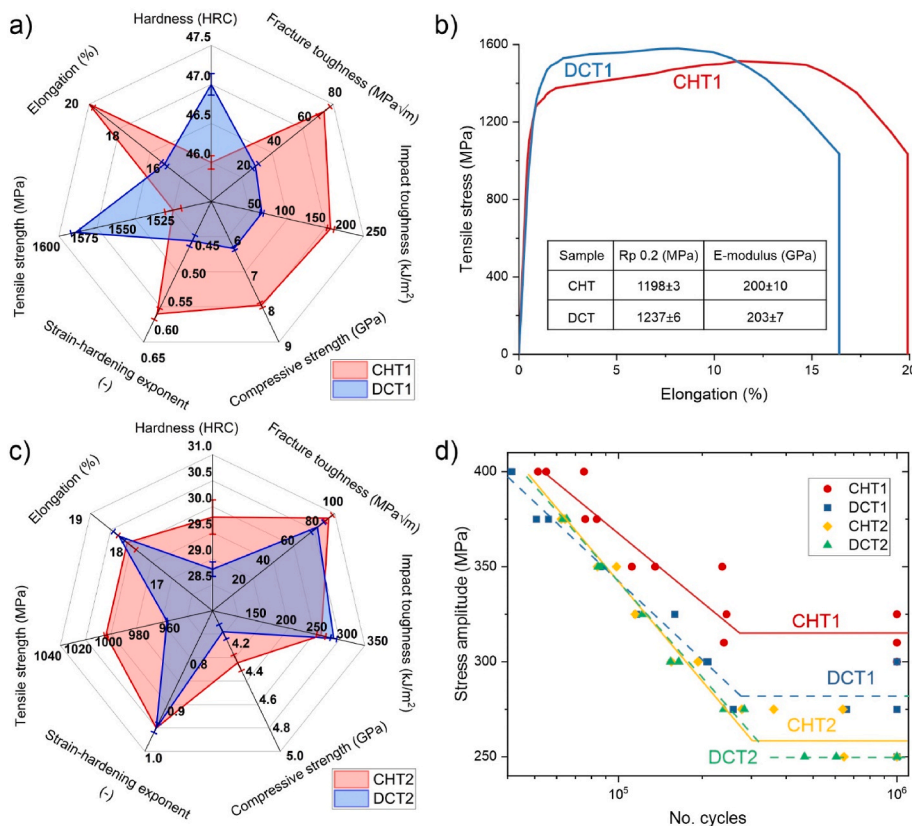


**Fig. 6.** (a) Spider web diagram illustrating the difference in mechanical properties between conventionally heat-treated (CHT1) and deep cryogenic treated (DCT1) samples. (b) Representative stress-strain curves of CHT1 and DCT1 samples with corresponding yield strength ( $R_{p0.2}$ ) and elastic modulus. (c) Spider web diagram illustrating the difference in mechanical properties between CHT2 and DCT2 samples. (d) Fatigue test results of all four groups of samples. The average trend of the fatigue response of each specimen group is shown by the connecting lines.

### 3.2. DCT impact on mechanical properties

The resulting microstructural changes have a distinct effect on the final mechanical properties of AISI 431. As can be seen from the graph in Fig. 6a, the hardness and strength of the DCT1 sample is higher compared to its CHT1 counterpart (from 46 HRC to 47 HRC and from 1525 MPa to 1589 MPa). This change is directly related to the reduced amount of austenite within the microstructure and the increased amount of martensite phase and carbides. However, as a result of the reduced amount of austenite, the material exhibits lower strain-hardening capabilities (from 0.6 to 0.47), lower compressive strength (from 7.95 GPa to 6.34 GPa) and reduced elongation (from 20% to 16.3%). In addition, the toughness of the DCT1 material is almost half that of the CHT1, which is also directly related to the significantly lower amount of austenite and increased amount of brittle martensite phases (both  $\alpha$  and  $\epsilon$ ). With the change in microstructure, the tensile stress-strain curve is also significantly altered with DCT. As can be seen in Fig. 6b, the DCT1 sample develops a higher yield strength as well as an offset in the achieved maximum strength per achieved strain. This correlates well with the much stronger and more homogeneous matrix material resulting from the higher presence of  $\alpha$ -martensite and  $\epsilon$ -martensite which allows the strength of the material to remain relatively constant with elongation. As such, the DCT1 material provides a combination of properties that are useful in the automotive industry to produce stiff frameworks required for safety in collisions, as well as for parts that need to withstand high loads without undergoing high plastic deformation [3,40, 41]. In contrast, the second heat treatment group shows significantly lower strength and hardness of both CHT2 and DCT2 compared to the first treatment group specimens. Furthermore, DCT2 slightly deteriorates in hardness (from 29.8 HRC to 28.8 HRC), tensile strength (from 1010 MPa to 970 MPa) and compressive strength (from 4.37 GPa to 4.15 GPa) compared to its CHT2 counterpart. On the other hand, elongation and work hardenability remain similar. Interestingly, DCT2 modifies the toughness of the material differently, inducing a slight improvement in impact toughness and a slight deterioration in fracture toughness. The significantly different effect of DCT on the mechanical properties resulting from the different treatment procedures strongly supports the strong correlation and dependence of DCT effectiveness on the selected heat treatment parameters of both austenitizing and tempering that have been reported for other steels [13,42,43].

## 4. Impact of DCT on fatigue and wear response of AISI 431

### 4.1. Fatigue

With DCT, the fatigue properties of AISI 431 are generally reduced

(see Fig. 6d). For the DCT1 group, this is clearly an effect of the reduced austenite content, which has a direct effect on impact and fracture toughness and thus the threshold for crack nucleation and propagation. Similarly, the DCT2 has a slightly lower fatigue limit than its CHT2 counterpart due to the lower fracture toughness. However, due to the higher impact toughness, the slope of the fatigue limit is similar for both CHT2 and DCT2 specimens. Further clarification of the effect of DCT on the cracking characteristics of AISI 431 is provided by fractographic analysis of the specimens (Fig. 7). The CHT1 specimen shows a highly ductile fracture that follows the high toughness of the specimen. In addition, high-resolution imaging reveals a dense network of small-scale pits connected by patches of highly deformed material (marked with arrows in Fig. 7a). The deformed patches and dimples are thought to be related to the high density of the austenite phase, which acts as a ductile buffer between the much stiffer martensitic matrix.

This is confirmed by the absence of such large formations in the DCT1 sample, which occur only in isolated areas as marked by the yellow arrows in Fig. 7c. In the brittle fracture regime (Fig. 7b and d), both CHT1 and DCT1 show the formation of deformation ridges (marked by dashed circles), which represent the local plastic deformation of individual grain boundaries. These are much more densely formed in the case of CHT1, further supporting its higher ductility compared to its DCT1 counterpart. In addition, the brittle regions indicate that the DCT1 sample exhibits clear fracturing across grain boundaries (marked by the yellow arrow in Fig. 7d). In contrast, the CHT1 sample shows a strong clustering of fatigue striations caused by dislocation agglomeration at localized barriers caused by the phase boundaries and grain boundaries of more ductile phases that can better resist cracking (example marked with yellow arrow in Fig. 7b). These fracture characteristics suggest that for the CHT1 sample, the matrix is the weak part that allows crack propagation, whereas for the DCT1 sample, the grain boundaries are the main weak sections through which the cracks nucleate and propagate. This clearly illustrates the reasons for the lower fatigue limit of the DCT1 specimen compared to its CHT1 counterpart.

Alternatively, the CHT2 and DCT2 specimens show a more similar and stronger deformation of the fractured material within the ductile regime, associated with the high fracture toughness of the second treatment group (see Fig. 6). Both specimens show ripples that follow the formation of individual plateaus (examples marked with yellow arrows in Fig. 7e and g). The plateaus are similar in size and morphology to the preceding austenite grains, suggesting that the grain boundaries decorated by the large carbides (see Fig. 5c–d) act as weakening points for crack propagation. From the brittle fracture region (Fig. 7f and h), the two samples show a significant difference. Namely, the DCT2 sample shows many voids left by torn out precipitated carbides. This suggests that the carbides in DCT2 are more densely formed and have also

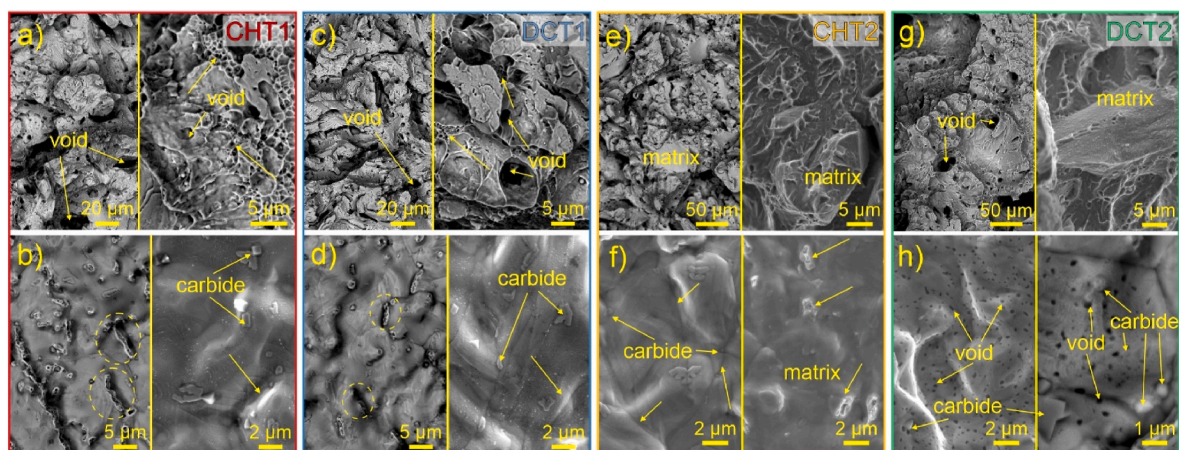


**Fig. 7.** SEM images of fracture surfaces of a-b) CHT1, c-d) DCT1, e-f) CHT2 and g-h) DCT2 samples. The upper images (a, c, e and g) correspond to the predominantly ductile fracture surfaces of the samples, while the lower images (b, d, f and h) correspond to the brittle portions of the fracture surfaces.

developed a more incoherent boundary with the matrix, resulting in faster crack initiation (lower fatigue limit) and compensated fatigue strength of the material due to the longer crack paths. In contrast, the CHT2 specimen shows similar ridge formation and preferential failure near grain boundaries as observed for the DCT specimen, supporting the conclusion that the grain boundaries decorated with the carbides act as weak points for crack initiation and propagation. These results are consistent with the denser and larger size of the carbides in DCT2 compared to CHT2 and with the advanced carbide precipitation as confirmed by microstructural characterization (see Fig. 5). Overall, despite the generally lower fatigue properties after DCT for both groups, the DCT AISI 431 retains considerably good fatigue properties comparable to other ultra-high strength AHSS [44,45].

#### 4.2. Wear resistance

Since the steels may be exposed to severe frictional conditions in the automotive industry, wear tests were performed under 4 dry sliding conditions against an  $\text{Al}_2\text{O}_3$  counterpart. The wear test results (Fig. 8) show a clear difference between the DCT and CHT variants of both heat treatment groups. Both DCT specimens exhibit a lower average steady-state coefficient of friction (COF) compared to their respective CHT counterparts, reaching values up to 25% lower (Fig. 8a). Consequently, a tendency towards a reduced wear rate (up to 2 times lower) is observed for both DCT sample groups compared to the corresponding CHT samples, regardless of the wear condition (Fig. 8b). The different conditions also show a general trend of increased COF with higher contact loads and higher sliding speeds. However, the wear rate shows an inverse relationship with respect to the contact conditions, particularly for CHT2 and DCT2 under low sliding conditions (Condition 1 and Condition 2). This is a strong indication that the friction conditions play a critical role in the wear mechanism of the material, regardless of the heat treatment process.

However, the exemplary evolution of the COF with time for the different specimens under condition 1, presented in Fig. 8c, clearly shows the strong influence of the DCT on the COF and thus on the reduced wear rate. For both DCT and DCT2, an initial low COF is

recorded, which is related to the higher resistance of the surface to cracking and deformation. For the DCT1 sample, the significantly lower COF is postulated to be due to the high hardness and low austenite content and the associated refinement of the martensitic microstructure, higher presence of  $\epsilon$ -martensite and increased carbide precipitation. This is also consistent with the significantly higher austenite content in the CHT1 sample, which allows for greater localized deformation of the material and thus cracking and spalling during wear. On the other hand, the DCT2 case is much less pronounced due to the much lower overall hardness for both CHT2 and DCT2. However, the lower initial COF is due to the refined microstructure and increased carbide precipitation, which locally strengthens the material and protects it from scaling.

The previously established relationship is further confirmed by SEM examination of the wear scars (Fig. 8d–e). The wear scars show that the DCT samples have less pronounced flaking and cracking of the material and abrasive wear formations at the edges of the wear scars (see Fig. 8e). In contrast, the CHT specimens show severe flaking and cracking of the material throughout, as shown in Fig. 8d. In addition, all specimens, whether CHT or DCT, develop similar wear phenomena and character in the central portion of the wear scars, mostly related to abrasive wear and oxidative wear. This supports that the material does not change the abrasive modes with DCT, but instead creates an offset in the development of the wear processes, requiring either longer exposures or more severe contact conditions to induce similar wear to those treated with CHT. This also strongly supports the lower initial COF for DCT samples in the wear tests.

#### 5. Discussion on DCT-induced microstructural transformations and CAR mechanism

All the results obtained indicate that DCT has a tremendous influence on the microstructure and thus on the properties of AISI 431 in the case of the first heat treatment group. In the case of the second group, the influence of DCT is less pronounced, but still allows certain modifications of the microstructure and thus of the properties studied. The greater influence of DCT in the first group is related to the suppression of austenite formation with subsequent tempering, as clearly shown by the

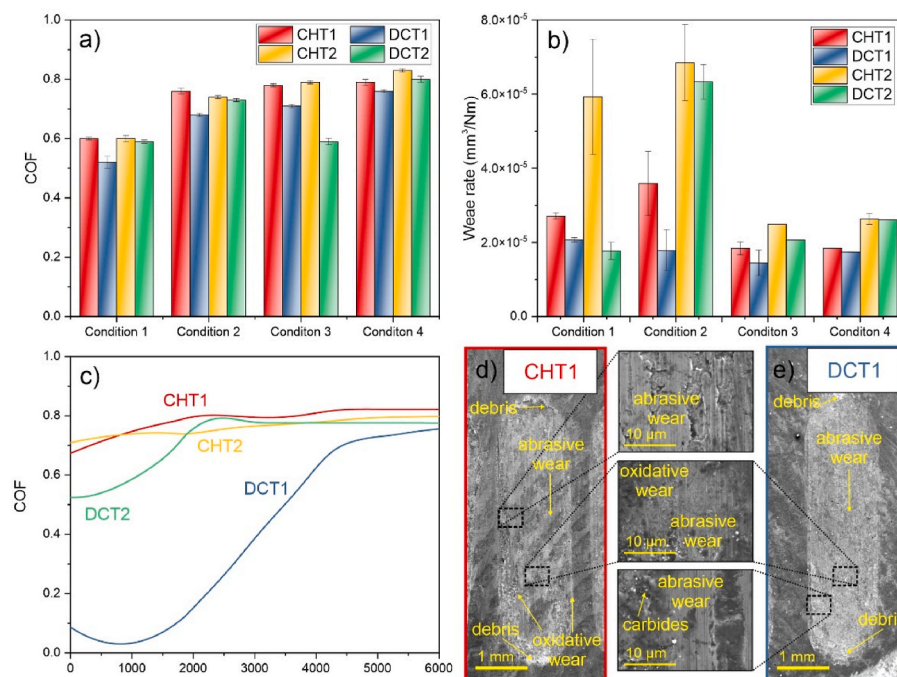


Fig. 8. Wear test results for each sample group of investigated AISI 431 steel: a) coefficient of friction (COF), b) wear rate and c) COF path of selected condition 1. Exemplary wear tracks obtained under condition 1 and imaged with SEM are shown in d) and e) for CHT1 and DCT1 samples, respectively.

ex-situ EBSD maps (see Fig. 3). The reason for the formation of austenite in the CHT sample is related to the ART effect that occurs due to the unstable state of the martensite. It is proposed that the instability arises from the locally high stress states of the material and localized inhomogeneities of the solute atoms after rapid quenching. These inhomogeneities give rise to two specific features. First, the highly strained martensite allows for increased microstructural partitioning by lowering the energetic barrier for preferential carbon segregation, resulting in localized carbon enrichments at martensitic lattice boundaries. These enrichments then activate the higher temperature instability of the martensitic regions to form the energetically favorable elongated austenite films at the martensitic lattice interface [46,47]. Secondly, the localized segregation of carbon within the martensitic laths results in the formation of carbides. This phenomenon produces carbides with elongated features that follow the main crystallographic axes of the martensite. This partitioning effect and subsequent carbide formation has been observed in similar martensitic stainless steels that also exhibit austenite reversion [46–49]. The microstructural process that develops during CHT is shown schematically in Fig. 9a (see CHT route).

However, in the case of DCT, the stress state of the material is relaxed and allows a higher stabilization of the microstructure formed by the dislocation pile-up, vacancy agglomeration and recombination of defects initiated by the shrinkage pressure [1,2]. The effect of the relaxed state of the material with DCT through reduced local inhomogeneities and stresses has been demonstrated for other steels and metallic materials [1,2,50,51]. However, this does not mean that carbon agglomerates are not present in the material, but that the energy landscape for the diffusion pathways is altered with preferential homogeneous redistribution throughout the bulk of the martensite matrix rather than further enhancement of local carbon agglomeration at phase boundaries. As a result, it is proposed that the corresponding stability of austenite with tempering is altered, leading to successive retransformation of austenite when prior DCT is performed. In the case of AISI 431, we propose that ART still occurs in the initial tempering stage, but is subsequently decomposed into refined martensite structures and carbides, which develop high stresses due to the local lattice mismatch. To compensate for the stress buildup effect, individual austenite strands are transformed into  $\varepsilon$ -martensite. This is supported by the higher formation of  $\varepsilon$ -martensite in groupings that follow a similar positioning of the austenite phase as found in the CHT counterpart (see Fig. 3). The phenomenon in principle originates at the same level as that of conventional TRIP, but that in this case the effect occurs at the microscopic level due

to the high localized microscopic stresses that provide the means for the decomposition of austenite and the formation of corresponding carbides and  $\varepsilon$ -martensite. We name this microstructural evolution and partitioning as Cryogenic Austenite Retransformation (CAR). This term will be used throughout the remainder of the manuscript for clarity and to separate it from the other effects. The full microstructural evolution and effects caused by DCT and CAR are shown schematically in Fig. 9a (see DCT route).

The CAR effect is particularly interesting because it provides a new microstructural transformation pathway different from those previously observed in similar steels [46,49,52]. In the case of CAR, treatment with DCT (immersion in LN<sub>2</sub>) removes or greatly reduces retained austenite and forms secondary martensite prior to tempering, as demonstrated in our previous publication [32]. This significantly different state of the material has a dominant effect on austenite formation during tempering as it effectively modifies carbon diffusion and redistribution during tempering. Yuan et al. [52] stated that the presence of reverted austenite allows further formation of reverted austenite and that the limited diffusivity of carbon in austenite is the main reason for stable austenite formation with tempering and/or partitioning of martensitic stainless steels. This is also clearly evident in AISI 431 due to the presence of a high amount of austenite in the CHT specimen and the absence of austenite in the CHT2 and DCT2 specimens due to the higher tempering temperature that allows sufficient thermal activation of carbon to occur and thus carbide enhanced formation and inability to form retained austenite (see Fig. 5). However, it should be noted that Song et al. [47] found high amounts of retained austenite even at temperatures as high as 580 °C. The difference may be due to the lower Ni content of AISI 431, which does not allow Ni enrichments [47] to form in the austenitic regions, which can further stabilize the austenite phase at high temperatures. Nevertheless, the DCT specimen initiates CAR, resulting in the loss of the austenite phase during tempering. Based on the present results, it can be assumed that the diffusivity of carbon is increased with the exposure to DCT. From our previous study [32] it is clear that despite the immersion in LN<sub>2</sub>, a small amount of austenite is still present in the sample. The slight presence of austenite is also confirmed by this study using magnetometry (see Fig. 5e). However, this could not be confirmed by EBSD mapping, which can be explained by the residual presence of nanoscopic austenite remnants determined by TEM (see Fig. 4e). Similar observations of nanoscopic presence of retained austenite after DCT were also reported by Kim et al. for Mn steels [53]. The presence of retained austenite in DCT AISI 431 then also supports that the CAR effect is ultimately a continuous transformation that occurs after ART is

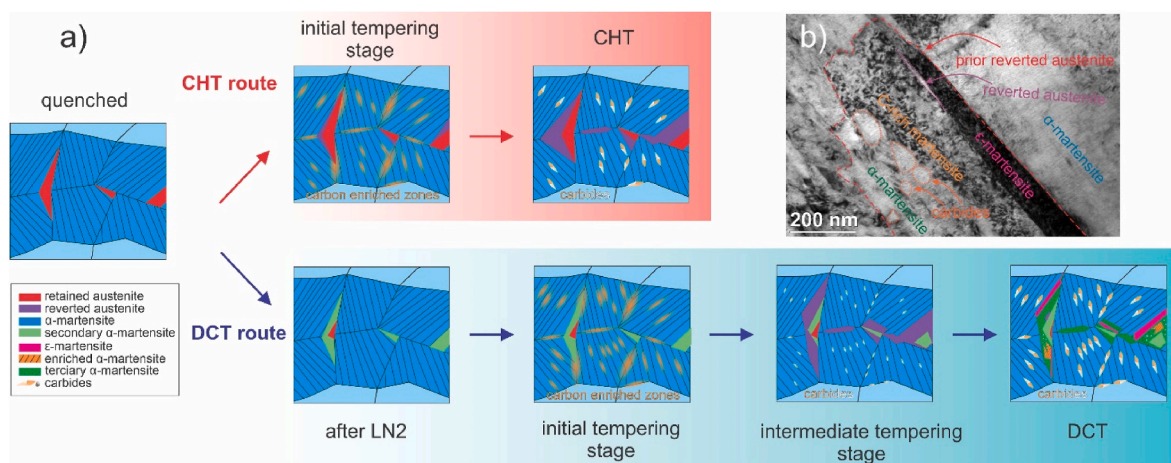


**Fig. 9.** a) Schematic representation of the microstructure evolution after conventional heat treatment (CHT) and deep cryogenic treatment (DCT) of AISI 431. b) Transmission electron micrograph showing the region of prior reverted austenite that develops a complex segmented microstructure after DCT and cryogenic austenite retransformation (CAR) as sketched in figure a). The corresponding phases and color-coded regions are described in the accompanying legend of a). (For interpretation of the references to color in this figure legend, the reader is referred to the Web version of this article.)

completed during the initial tempering stage (see DCT path in Fig. 9a). Thus, we postulate that the formation of reverted austenite still occurs within AISI 431, but is later partitioned into the different martensite substructures due to the higher diffusivity of carbon and the instability of austenite with prolonged tempering time.

Closer examination of the TEM data reveals the possible relationship of the segmented microstructural features to the previously reverted austenite, as shown in Fig. 9b. The regions near the darker  $\epsilon$ -martensite bands (left and right) show a strong contrast difference, although both regions are crystallographically determined to be  $\alpha$ -martensite. Using local EDS (see Table 3), it was found that the darkened  $\alpha$ -martensite regions contain considerable amounts of carbon, in the range of the carbon content of residual austenite. The carbon content in both phases far exceeds the expected concentration of 0.4 wt% calculated thermodynamically for retained austenite at equilibrium under selected heat treatment conditions. The carbon enrichment for austenite is expected due to the high solubility of carbon in austenite and the limited diffusivity of carbon within austenite expected in non-equilibrium states of steels [52,54]. However, the enriched martensite after such a long tempering time is unprecedented. The clearly enriched and stable martensite regions can only be understood by the local high lattice strain of the material caused by the sudden transformation of austenite into tertiary  $\alpha$ -martensite and  $\epsilon$ -martensite. This has been reported in other studies as a possible reason for enhanced or retarded carbon diffusion based on local elastic stresses of individual phases [55], as well as enhanced dislocation pinning at carbon-rich zones and phases [56,57]. Furthermore, the  $\gamma \rightarrow \epsilon$  transformation allows for high dislocation generation in localized regions, leading to high dislocation density and thus increased local stresses that can stabilize carbon-rich phases [58]. The TEM image in Fig. 9b provides a correlation to the previously reverted austenite (marked by red dashed lines), which is locally partitioned into the different martensite phases and carbides. The C-rich  $\alpha$ -martensite is trapped between the remaining austenite and  $\epsilon$ -martensite on one side and by the large cluster of carbides on the other. This has the potential to explain the localized enrichment due to diffusion barriers caused by the different phases. This is further supported by the high carbon content of 0.8 wt% of  $\epsilon$ -martensite, which follows the relationship with the previous reverted austenite, made possible by the inherent retention of carbon after transformation [59]. It is proposed that the interphase formation of carbides and segregation of carbon to other carbon-rich regions is the reason for the lower carbon content in  $\epsilon$ -martensite due to the faster diffusion of carbon in  $\epsilon$ -martensite than in austenite during tempering. This in turn creates a gradient in the stacking fault energy due to the different carbon content and stress state, which in turn creates the different stability potential of each phase. Similar results have been reported for Mn steels [54]. In addition, the gradient of carbon content and transformation kinetics into different phases also follows the general trend of directional transformation of martensite and austenite in martensitic stainless steels [46]. From all of the above, it is clear that DCT, with the associated CAR effect, provides a complex and finely sectioned multiphase microstructure that allows the development and tailoring of mechanical properties, especially in relation to the plastic

deformation response, as observed in this study, and may have a similar tuning capability with different heat treatment processes as that of Mn steels [60].

From the EDS measurements it can also be concluded that carbon plays the dominant role in the segregation of the different phases, since Cr does not show significant differences between the different phases due to its limited diffusibility. The only additional element is Ni, which shows a slight enrichment in the austenite phase compared to the martensite phases, which is consistent with the higher Ni content in austenite reported by Song et al. [47] and may be a possible reason for the higher stability of the nano-sized austenite regions after DCT due to the limited diffusivity of Ni. Since the individual matrix phases do not show much variation in the alloying elements, it is reasonable to assume that the formation of carbides is also generally driven by local carbon diffusivity. This also implies that critical nucleation based on local energy landscapes and chemical potentials associated with carbon drives the phase transformations rather than agglomeration of other alloying elements. It is also clear that Cr-based martensitic stainless steels exhibit a different DCT-induced nanoscopic carbide formation mechanism than martensitic steels with other alloying elements and thermal treatments [32,38].

While CAR explains the change in austenite fraction and subsequent formation of a complex martensitic matrix, the increased carbide precipitation of the DCT1 sample compared to the CHT1 sample is due to the general DCT effect on carbide precipitation as found in other steels [9,32,38,61–63]. In general, the resulting dislocation pile-ups and vacancy agglomerations formed after DCT act as nucleation sites for new carbides through enhanced alloy segregation activated by subsequent tempering [38]. This leads to a predominant formation of nanoscopic carbides that form throughout the bulk of the material, thereby increasing the strength and hardness of the material and allowing additional subdivision of the martensitic matrix during tempering [1]. The effect of dislocations and vacancies on  $M_{23}C_6$  carbide precipitation in AISI 431, as calculated by thermodynamic calculations using ThermoCalc, is shown in Fig. 10a–b. The calculations illustrate the strong influence of bulk activated precipitation on carbide formation. By considering the bulk precipitation as the dominant form of carbide formation in the case of DCT, whereas in CHT the nucleation and growth of carbides is excessively formed at grain boundaries, the volume fraction of carbides should be higher up to 3% in the case of DCT. This is in good agreement with the increased carbide fraction found in the DCT samples determined both by microscopic observations (see Section 3.1) and by the 2 vol% increase in carbides determined by XRD [32] compared to the CHT variant. It should be noted that this precipitation improvement is only related to the general increase in  $M_{23}C_6$  carbides and not to the additional  $M_3C$  carbides formed due to the austenite partitioning caused by CAR.

## 6. Prospects of deep-cryogenic treated AISI 431

With the understanding of the underlying mechanism and further tuning of the effects of DCT and CAR on AISI 431, the steel has a strong

**Table 3**

Local EDS measurements of different phases found in the DCT sample with included standard deviation (SD). The individual phases are shown and labelled in the TEM micrograph in Fig. 9b.

	$\alpha$ -martensite	SD	C-rich $\alpha$ -martensite	SD	austenite	SD	$\epsilon$ -martensite	SD
C	0.15	0.03	1.77	0.08	1.83	0.09	0.83	0.18
Al	0.19	0.01	0	0	0.11	0.02	0.02	0
Si	0.43	0.36	0.24	0.12	0.72	0.22	0.37	0.14
Cr	15.74	0.02	15.47	0.01	15.26	0.02	15.47	0.02
Mn	1.45	0.08	1.06	0.02	1.34	0.03	1.41	0.19
Fe	80.27	0.1	79.13	0	79.05	0	80.1	0
Ni	1.5	0.15	1.52	0.18	1.61	0.22	1.5	0.21
Cu	0.27	0.01	0.35	0.04	0.09	0.01	0.28	0.01
Mo	0	0	0.46	0.02	0	0	0	0

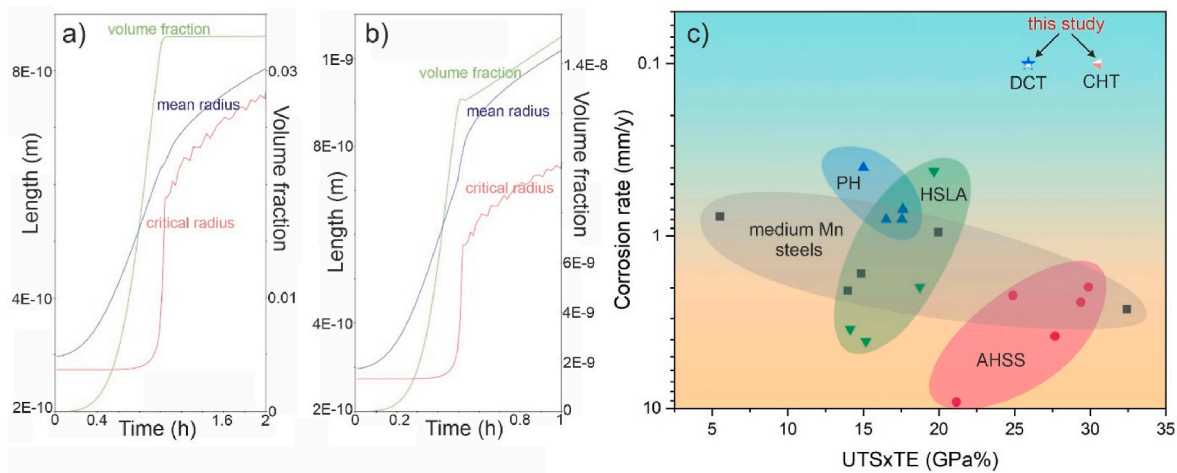


**Fig. 10.** Thermodynamically calculated precipitation of  $M_{23}C_6$  carbides in AISI 431 in relation to a) bulk and b) dislocation governed carbide nucleation and growth during tempering at 480 °C. c) Comparative map plot showing the placement of the current cryogenically heat-treated (DCT1) and conventionally heat-treated (CHT1) AISI 431 from this study in relation to the corrosion resistance (evaluated by corrosion rate in NaCl [64–75] and product of ultimate tensile strength (UTS) and tensile elongation (TE) of medium Mn-steels, precipitation hardening steels (PH), high-strength low-alloy (HSLA) steels and advanced high-strength steels (AHSS) that are commonly used in the automotive industry [65,76–80]. The corrosion rate of AISI 431 is set to the values obtained from Ref. [81].

prospect to be utilized as a next generation AHSS. While the steel exhibits significantly high strength and elongation, providing high strain energy comparable to other 3rd generation AHSS (see Fig. 10c), the steel also provides a significantly important aspect in terms of corrosion resistance. Unlike other 3rd generation AHSS, Mn steels, HSLA and PH steels (see Fig. 10c), AISI 431 offers significantly higher corrosion resistance due to its high chromium content. The fact that the steel has high strength, high elongation and high corrosion resistance is particularly important for the sustainable development of future automotive components, which would not require specific corrosion resistant coatings and zinc anodizing [82,83], compared to the current Mn steels, which suffer from much lower corrosion resistance [84]. Furthermore, since galvanizing can potentially cause further embrittlement of steels and their surfaces via liquid metal embrittlement [85], this effect can be avoided by using AISI 431-like steels. In addition, the material has shown an exceptional ability to tailor mechanical properties and tensile response with DCT. On the one hand, the material can provide exceptional elongation and toughness when treated with CHT, but on the other hand, increased strength, hardness and higher deformation resistance can be achieved with DCT. The combination of the two can open up new possibilities for the design of body parts without the use of welding. To this end, AISI 431 can be used in a similar way as proposed by Lu et al. [86], which we have already shown in this study by using two different heat treatment parameterizations that can provide significantly different properties needed for different body parts [86]. However, unlike the Unisteel of Lu et al. [86], AISI 431 provides significantly higher strain energy as well as higher corrosion resistance. In addition, DCT offers the possibility of avoiding welding of certain adjacent parts with significantly different properties by tailoring the DCT effect with respect to individual treatment procedures and parameters. In practice, sectional treatment of individual parts with  $LN_2$  can be performed by cryogenic tunneling [87] or cryogenic spraying [88,89], which can provide controllable sectional treatment of individual parts that are then heat treated together, but provide different final properties within the same workpiece. In addition, as seen in relation to wear resistance (see Fig. 8), surface hardening and increased wear resistance of the material can also be achieved with prior surface cooling. This in turn allows the development of a sophisticated material structure that can be easily controlled and treated by a single heat treatment process. In addition, the alloying of AISI 431 allows the alloy to be priced at around \$1000 per ton, which is at the lower cost end of the ultra-high strength steels [90]. In addition, due to the low Ni content and the predominant Cr

alloying, the steel is also very attractive from a sustainability point of view, as it delivers an abundance risk of around 0.27, which is one of the lowest values within the group of ultrahigh strength steels [90].

## 7. Conclusions

In this work, we have studied the impact of deep cryogenic treatment (DCT) on the properties of AISI 431, which are modified due to the substantially altered microstructure of the studied martensitic stainless steel. The microstructural changes result from the subsequent transformation of the reverted austenite that occurs during the initial quenching and tempering process due to austenite reversion transformation (ART). Based on ex-situ microstructural evaluations, we conclude that the reverted austenite is further retransformed into  $\alpha$ -martensite,  $\epsilon$ -martensite, and carbides in the form of intricate microscopic regions during tempering. We discuss the novel mechanism, which we have termed Cryogenic Austenite Retransformation (CAR), that results from the build-up of localized stresses and altered carbon diffusion within the initial microstructure prior to tempering due to prior exposure of the material to cryogenic temperatures. With the activation of CAR by DCT, the resulting microstructure provides improved material strength combined with good ductility, resulting in a stronger and more deformation resistant material compared to the conventionally heat treated (CHT) variant at comparable total strain energy. However, the improvement with DCT comes at the expense of reduced toughness and fatigue resistance. Nevertheless, the toughness and fatigue resistance of DCT AISI 431 are still competitive to most AHSSs with similar strengths and deformation energies. From fractographic analysis, we conclude that the increased brittleness of the DCT specimens is due to increased carbide growth at grain boundaries and the absence of the austenite phase that would act as a buffer for crack propagation and stress buildup. Additionally, DCT provides a significant improvement, up to 25%, in the wear resistance of AISI 431, which is related to the much slower evolution of the wear processes and the reduced coefficient of friction induced by the higher presence of harder microstructural phases (martensite phases and carbides).

The effect of DCT is also studied in relation to different heat treatment parameters (lower austenitizing and higher tempering temperature), which still gives an improvement of some properties with DCT, but in a much less pronounced way. It is concluded that this occurs because AISI 431 lacks ART due to the higher tempering temperature. This inevitably confirms that the ART effect is crucial for the dramatic

tailoring of microstructure and properties with DCT in the first treatment case. The general improvement in individual properties for both cases is due to the refinement of the martensitic matrix and subsequent enhanced carbide precipitation that is commonly reported for DCT steels. These results present DCT as a reliable tool for modifying the microstructure and properties of AISI 431 and similar steels under different heat treatments and can provide additional property tailoring that would not be possible with conventional treatments. In addition, the relatively simple approach of microstructure tailoring with DCT provides a novel route to advanced 3rd generation high strength steels while utilizing existing low cost and abundant steels that previously could not provide sufficient properties and behavior. With our study, we have so far provided the fundamental understanding of the DCT effect on AISI 431 and its tremendous impact through novel microstructural mechanisms, which still has great potential to be further tailored and improved with further studies and systematic modification of the treatment regimes.

From all of the above, we conclude that AISI 431 and similar steels represent a great opportunity for the development of the next generation AHSS group that also has a reasonable economic and sustainable character, while offering excellent corrosion properties, mechanical properties as well as flexibility in processing through the use of different treatment processes such as DCT. With DCT, the range of properties of AISI 431 can be extended to various applications and components in the automotive industry and beyond.

## Funding

This work was supported by Slovenian Research Agency (ARRS), Ljubljana, Slovenia [No. P2-0050 and P2-0132].

## CRedit authorship contribution statement

**Patricia Jovičević-Klug:** Conceptualization, Methodology, Investigation, Visualization, Resources, Writing – original draft, Writing – review & editing. **Matic Jovičević-Klug:** Conceptualization, Methodology, Investigation, Visualization, Writing – original draft, Writing – review & editing. **Lars Thormählen:** Methodology, Writing – review & editing. **Jeffrey McCord:** Supervision, Resources, Writing – review & editing. **Michael Rohwerder:** Supervision, Resources, Writing – review & editing. **Matjaž Godec:** Supervision, Resources, Writing – review & editing. **Bojan Podgornik:** Supervision, Resources, Writing – review & editing. All authors have read and agreed to the published version of the manuscript.

## Declaration of competing interest

The authors declare that they have no known competing financial interests or personal relationships that could have appeared to influence the work reported in this paper.

## Data availability

Data will be made available on request.

## Acknowledgement

The authors acknowledge the technical and scientific assistance of Institute of Metals and Technology, Slovenia and Max-Planck-Institute for Iron Research, Germany.

## Appendix A. Supplementary data

Supplementary data to this article can be found online at <https://doi.org/10.1016/j.msea.2023.145033>.

## References

- [1] P. Jovičević-Klug, L. Tegg, M. Jovičević-Klug, R. Parmar, M. Amati, L. Gregoratti, L. Alması, J.M. Cairney, B. Podgornik, Understanding carbide evolution and surface chemistry during deep cryogenic treatment in high-alloyed ferrous alloy, *Appl. Surf. Sci.* 610 (2023), 155497, <https://doi.org/10.1016/j.apusc.2022.155497>.
- [2] P. Jovičević-Klug, M. Jovičević-Klug, L. Tegg, D. Seidler, L. Thormählen, R. Parmar, M. Amati, L. Gregoratti, J.M. Cairney, J. McCord, M. Rohwerder, B. Podgornik, Correlative surface and bulk analysis of deep cryogenic treatment influence on high-alloyed ferrous alloy, *J. Mater. Res. Technol.* 11–12 (2022) 4799–4810.
- [3] F. Kara, Y. Küçük, O. Özbek, N.A. Özbek, M.S. Gök, E. Altaş, İ. Uygur, Effect of cryogenic treatment on wear behavior of Slepner cold work tool steel, *Tribol. Int.* 180 (2023), 108301, <https://doi.org/10.1016/j.triboint.2023.108301>.
- [4] V.G. Gavriljuk, W. Theisen, V.v. Sirosh, E.v. Polshin, A. Kortmann, G.S. Mogilny, Y.N. Petrov, Y.v. Tarusin, Low-temperature martensitic transformation in tool steels in relation to their deep cryogenic treatment, *Acta Mater.* 61 (2013) 1705–1715, <https://doi.org/10.1016/j.actamat.2012.11.045>.
- [5] A.I. Tyshchenko, W. Theisen, A. Oppenkowski, S. Siebert, O.N. Razumov, A. P. Skoblik, V.A. Sirosh, Y.N. Petrov, V.G. Gavriljuk, Low-temperature martensitic transformation and deep cryogenic treatment of a tool steel, *Mater. Sci. Eng.* 527 (2010) 7027–7039, <https://doi.org/10.1016/j.msea.2010.07.056>.
- [6] H. huai Liu, J. Wang, B. lu Shen, H. shan Yang, S. ji Gao, S. jiu Huang, Effects of deep cryogenic treatment on property of 3Cr13Mo1V1.5 high chromium cast iron, *Mater. Des.* 28 (2007) 1059–1064, <https://doi.org/10.1016/j.matdes.2005.09.007>.
- [7] M. Jovičević-Klug, R. Rezar, P. Jovičević-Klug, B. Podgornik, Influence of deep cryogenic treatment on natural and artificial aging of Al-Mg-Si alloy EN AW 6026, *J. Alloys Compd.* 899 (2022), 163323, <https://doi.org/10.1016/j.jallcom.2021.163323>.
- [8] M. Jovičević-Klug, L. Tegg, P. Jovičević-Klug, G. Dražić, L. Almásy, B. Lim, J. M. Cairney, B. Podgornik, Multiscale modification of aluminum alloys with deep cryogenic treatment for advanced properties, *J. Mater. Res. Technol.* 21 (2022) 3062–3073, <https://doi.org/10.1016/j.jmrt.2022.10.089>.
- [9] P. Jovičević-Klug, A.Z. Guštin, M. Jovičević-Klug, B. Šetina Batič, A. Lebar, B. Podgornik, Coupled role of alloying and manufacturing on deep cryogenic treatment performance on high-alloyed ferrous alloys, *J. Mater. Res. Technol.* 18 (2022) 3184–3197, <https://doi.org/10.1016/j.jmrt.2022.04.025>.
- [10] P. Jovičević-Klug, G. Puš, M. Jovičević-Klug, B. Žužek, B. Podgornik, Influence of heat treatment parameters on effectiveness of deep cryogenic treatment on properties of high-speed steels, *Mater. Sci. Eng., A* 829 (2022), 142157, <https://doi.org/10.1016/j.msea.2021.142157>.
- [11] D. Senthilkumar, Influence of deep cryogenic treatment on hardness and toughness of En31 steel, *Adv. Mater. Process. Technol.* 5 (2019) 114–122, <https://doi.org/10.1080/2374068X.2018.1530426>.
- [12] A. Idayan, A. Gnanavelbabu, K. Rajkumar, Influence of deep cryogenic treatment on the mechanical properties of AISI 440C bearing steel, in: *Procedia Eng*, Elsevier Ltd, 2014, pp. 1683–1691, <https://doi.org/10.1016/j.proeng.2014.12.319>.
- [13] Z. Yan, K. Liu, J. Eckert, Effect of tempering and deep cryogenic treatment on microstructure and mechanical properties of Cr–Mo–V–Ni steel, *Mater. Sci. Eng.* 787 (2020), 139520, <https://doi.org/10.1016/j.msea.2020.139520>.
- [14] P. Jovičević-Klug, M. Jovičević-Klug, M. Rohwerder, M. Godec, B. Podgornik, Complex interdependency of microstructure, mechanical properties, fatigue resistance and residual stress of austenitic stainless steels AISI 304L, *J. Mater. Res. Technol.* (2023). *Progress*.
- [15] C.H. Nanasa, M. Jahazi, Simultaneous enhancement of strength and ductility in cryogenically treated AISI D2 tool steel, *Mater. Sci. Eng.* 598 (2014) 413–419.
- [16] Z. Weng, K. Gu, K. Wang, X. Liu, J. Wang, The reinforcement role of deep cryogenic treatment on the strength and toughness of alloy structural steel, *Mater. Sci. Eng., A* 772 (2020), 138698, <https://doi.org/10.1016/j.msea.2019.138698>.
- [17] Z. Yang, Z. Liu, J. Liang, Z. Yang, G. Sheng, Elucidating the role of secondary cryogenic treatment on mechanical properties of a martensitic ultra-high strength stainless steel, *Mater. Char.* 178 (2021), 111277, <https://doi.org/10.1016/j.matchar.2021.111277>.
- [18] I. Saefuloh, N. Kanani, F.G. Ramadhan, Y. Rukmayadi, Y. Yusuf, S. Abdullah, S. Susilo, The study of corrosion behavior and hardness of AISI stainless steel 304 in concentration of chloride acid solution and temperature variations, *J. Phys. Conf. Ser.* 1477 (2020), 052058, <https://doi.org/10.1088/1742-6596/1477/5/052058>.
- [19] P. Jovičević-Klug, M. Jovičević-Klug, B. Podgornik, Unravelling the role of nitrogen in surface chemistry and oxidation evolution of deep cryogenic treated high-alloyed ferrous alloy, *Coatings* 12 (2022) 213, <https://doi.org/10.3390/coatings12020213>.
- [20] J. Voglar, Ž. Novak, P. Jovičević-Klug, B. Podgornik, T. Kosec, Effect of deep cryogenic treatment on corrosion properties of various high-speed steels, *Metals* 11 (2020) 14, <https://doi.org/10.3390/met11010014>.
- [21] P. Jovičević-Klug, M. Sedlaček, M. Jovičević-Klug, B. Podgornik, Effect of deep cryogenic treatment on wear and galling properties of high-speed steels, *Materials* 14 (2021) 1–16, <https://doi.org/10.3390/met11010014>.
- [22] I. Gunes, A. Cicek, K. Aslantas, F. Kara, Effect of deep cryogenic treatment on wear resistance of AISI 52100 bearing steel, *Trans. Indian Inst. Met.* 67 (2014) 909–917, <https://doi.org/10.1007/s12666-014-0417-4>.
- [23] M. Jovičević-Klug, P. Jovičević-Klug, T. Kranjec, B. Podgornik, Cross-effect of surface finishing and deep cryogenic treatment on corrosion resistance of AISI M35

- steel, *J. Mater. Res. Technol.* 14 (2021) 2365–2381, <https://doi.org/10.1016/j.jmrt.2021.07.134>.
- [24] P. Jovičević-Klug, T. Kranjec, M. Jovičević-Klug, T. Kosec, B. Podgornik, Influence of the deep cryogenic treatment on AISI 52100 and AISI D3 steel's corrosion resistance, *Materials* 14 (2021) 6357, <https://doi.org/10.3390/MA14216357>, 14 (2021) 6357.
- [25] A. Weidner, *Deformation Processes in TRIP/TWIP Steels: In-Situ Characterization Techniques*, 2020, p. 295, <https://doi.org/10.1007/978-3-030-37149-4>.
- [26] T. Kumar, A. Khullar, S. Suresh, A. Biswal, V. v Mahashabde, *Advanced High Strength Steel: Processing and Applications*, 2018.
- [27] M.Y. Demeri, *Advanced High-Strength Steels: Science, Technology, and Applications*, ASM International, Materials Park, OH, USA, 2013.
- [28] M. Bhargava, S. Chakrabarty, V.K. Barnwal, A. Tewari, S.K. Mishra, Effect of microstructure evolution during plastic deformation on the formability of transformation induced plasticity and quenched & partitioned AHSS, *Mater. Des.* 152 (2018) 65–77, <https://doi.org/10.1016/j.matdes.2018.04.068>.
- [29] S. Prabhudev, S. Swaminathan, M. Rohwerder, Effect of oxides on the reaction kinetics during hot-dip galvanizing of high strength steels, *Corrosion Sci.* 53 (2011) 2413–2418, <https://doi.org/10.1016/j.corsci.2011.03.027>.
- [30] L. Gu, Z. Wang, Y. Zhang, A. Guo, D. Stalheim, Development and application of the high-strength wear-resistance steel used for the lightweight heavy-duty dump mining truck, in: *HSLA Steels 2015*, Microalloying 2015 & Offshore Engineering Steels, 2015. Springer 978-3-319-48614-7, USA, n.d.
- [31] A. Rajesekhar, Heat treatment methods applied to AISI 431 martensitic stainless steels, *Int. J. Sci. Eng. Res.* 6 (2015) 547–553.
- [32] P. Jovičević-Klug, M. Jovičević-Klug, T. Sever, D. Feizpour, B. Podgornik, Impact of steel type, composition and heat treatment parameters on effectiveness of deep cryogenic treatment, *J. Mater. Res. Technol.* 14 (2021) 1007–1020.
- [33] P. Jovičević-Klug, N. Lipovšek, M. Jovičević-Klug, B. Podgornik, Optimized preparation of deep cryogenic treated steel and Al-alloy samples for optimal microstructure imaging results, *Mater. Today Commun.* 27 (2021), 102211, <https://doi.org/10.1016/j.mtcomm.2021.102211>.
- [34] B. Podgornik, B. Žužek, V. Leskovešek, Experimental evaluation of tool steel fracture toughness using circumferentially notched and precracked tension bar specimen, *Mater. Perform. Charact.* 3 (2014) 87–103.
- [35] D. Panov, E. Kudryavtsev, R. Chernichenko, A. Smirnov, N. Stepanov, Y. Simonov, S. Zherebtsov, G. Salishchev, Mechanisms of the reverse martensite-to-austenite transformation in a metastable austenitic stainless steel, *Metals* 11 (2021), <https://doi.org/10.3390/met11040599>.
- [36] V. Sagaradze, S. Afanasiev, N. Kataeva, Y. Ustyugov, Microstructure, phase transformations, and mechanical properties of shape memory Fe-Mn-V-C austenitic steels, *Metals* 13 (2023) 248, <https://doi.org/10.3390/MET13020248>, 13 (2023) 248.
- [37] P. Hedström, U. Lienert, J. Almer, M. Odén, Elastic strain evolution and e-martensite formation in individual austenite grains during in situ loading of a metastable stainless steel, *Mater. Lett.* 62 (2008) 338–340, <https://doi.org/10.1016/j.matlet.2007.05.054>.
- [38] P. Jovičević-Klug, M. Jovičević-Klug, B. Podgornik, Effectiveness of deep cryogenic treatment on carbide precipitation, *J. Mater. Res. Technol.* 9 (2020) 13014–13026, <https://doi.org/10.1016/j.jmrt.2020.09.063>.
- [39] M. Jovicvic-Klug, P. Jovicvic-Klug, J. McCord, B. Podgornik, Investigation of microstructural attributes of steel surfaces through magneto-optical Kerr effect, *J. Mater. Res. Technol.* 11 (2021) 1245–1259, <https://doi.org/10.1016/j.jmrt.2021.01.106>.
- [40] P. Jovičević-Klug, B. Podgornik, Review on the effect of deep cryogenic treatment of metallic materials in automotive applications, *Metals* 10 (2020) 434, <https://doi.org/10.3390/met10040434>.
- [41] V.R.M. Gonçalves, B. Podgornik, V. Leskovešek, G.E. Totten, L. de C.F. Canale, Influence of deep cryogenic treatment on the mechanical properties of spring steels, *J. Mater. Eng. Perform.* 28 (2019) 769–775, <https://doi.org/10.1007/S11665-019-3864-6>/FIGURES/12.
- [42] L. Tóth, F. Réka, The effects of quenching and tempering treatment on the hardness and microstructures of a cold work steel, *Int. J. Eng. Manag. Sci.* 4 (2019) 286–294, <https://doi.org/10.21791/ijems.2019.1.36>.
- [43] J.D. Darwin, D. Mohan Lal, G. Nagarajan, Optimization of cryogenic treatment to maximize the wear resistance of 18% Cr martensitic stainless steel by Taguchi method, *J. Mater. Process. Technol.* 195 (2008) 241–247, <https://doi.org/10.1016/j.jmatprotec.2007.05.005>.
- [44] J.G. Sezgün, J. Yamabe, Tensile and fatigue properties of 17-4PH martensitic stainless steels in presence of hydrogen, *Procedia Struct. Integr.* 19 (2019) 249–258, <https://doi.org/10.1016/j.prostr.2019.12.027>.
- [45] S. Kim, D. Jeong, H. Sung, Reviews on factors affecting fatigue behavior of high-Mn steels, *Met. Mater. Int.* 24 (2018) 1–14, <https://doi.org/10.1007/S12540-017-7459-1>, 1. 24 (2018).
- [46] F. Niessen, Austenite reversion in low-carbon martensitic stainless steels – a CALPHAD-assisted review, 1401–1414. 34, <https://doi.org/10.1080/02670836.2018.1449179>, 2018.
- [47] Y.Y. Song, X.Y. Li, L.J. Rong, Y.Y. Li, T. Nagai, Reversed austenite in OCr13Ni4Mo martensitic stainless steels, *Mater. Chem. Phys.* 143 (2014) 728–734, <https://doi.org/10.1016/j.matchemphys.2013.10.006>.
- [48] S.Y. Lu, K.F. Yao, Y.B. Chen, M.H. Wang, N. Chen, X.Y. Ge, Effect of quenching and partitioning on the microstructure evolution and electrochemical properties of a martensitic stainless steel, *Corrosion Sci.* 103 (2016) 95–104, <https://doi.org/10.1016/j.corsci.2015.11.010>.
- [49] P. Wang, W. Zheng, X. Yu, Y. Wang, Advantageous implications of reversed austenite for the tensile properties of super 13Cr martensitic stainless steel, *Materials* 15 (2022) 7697, <https://doi.org/10.3390/MA15217697>, 15 (2022) 7697.
- [50] L.Y. Xu, J. Zhu, H.Y. Jing, L. Zhao, X.Q. Lv, Y.D. Han, Effects of deep cryogenic treatment on the residual stress and mechanical properties of electron-beam-welded Ti–6Al–4V joints, *Mater. Sci. Eng.* 673 (2016) 503–510, <https://doi.org/10.1016/j.msea.2016.07.101>.
- [51] D. Senthilkumar, Effect of deep cryogenic treatment on residual stress and mechanical behaviour of induction hardened En 8 steel, *Adv. Mater. Process. Technol.* 2 (2016) 427–436, <https://doi.org/10.1080/2374068X.2016.1244326>.
- [52] L. Yuan, D. Ponge, J. Wittig, P. Choi, J.A. Jiménez, D. Raabe, Nanoscale austenite reversion through partitioning, segregation and kinetic freezing: example of a ductile 2 GPa Fe–Cr–C steel, *Acta Mater.* 60 (2012) 2790–2804, <https://doi.org/10.1016/j.actamat.2012.01.045>.
- [53] D.W. Kim, J. Yoo, S.S. Sohn, S. Lee, Austenite reversion through subzero transformation and tempering of a boron-doped strong and ductile medium-Mn lightweight steel, *Mater. Sci. Eng., A* 802 (2021), 140619, <https://doi.org/10.1016/j.msea.2020.140619>.
- [54] Y.F. Shen, X.X. Dong, X.T. Song, N. Jia, Carbon content-tuned martensite transformation in low-alloy TRIP steels, *Sci. Rep.* 9 (2019) 1–9, <https://doi.org/10.1038/s41598-019-44105-6>, 1. 9 (2019).
- [55] I. Steinbach, M. Apel, The influence of lattice strain on pearlite formation in Fe–C, *Acta Mater.* 55 (2007) 4817–4822, <https://doi.org/10.1016/j.actamat.2007.05.013>.
- [56] Z. Liu, S. Zhang, S. Wang, Y. Feng, Y. Peng, J. Gong, M.A.J. Somers, Redistribution of carbon and residual stress in low-temperature gaseous carburized austenitic stainless steel during thermal and mechanical loading, *Surf. Coat. Technol.* 426 (2021), 127809, <https://doi.org/10.1016/j.surfcoat.2021.127809>.
- [57] C. Kremaszky, U. Liedl, E.A. Werner, A note on the diffusion of carbon atoms to dislocations, *Comput. Mater. Sci.* 38 (2006) 90–97, <https://doi.org/10.1016/j.commatsci.2006.01.010>.
- [58] V.v. Sagaradze, V.E. Danilchenko, P. L'Heritier, V.A. Shabashov, The structure and properties of Fe–Ni alloys with a nanocrystalline austenite formed under different conditions of  $\gamma$ - $\alpha$  transformations, *Mater. Sci. Eng., A* 337 (2002) 146–159, [https://doi.org/10.1016/S0921-5093\(02\)00023-0](https://doi.org/10.1016/S0921-5093(02)00023-0).
- [59] V.E. Danilchenko, A.v. Filatov, V.F. Mazanko, V.E. Iakovlev, Cyclic martensitic transformations influence on the diffusion of carbon atoms in Fe-18 wt.%Mn-2 wt.%Si alloy, *Nanoscale Res. Lett.* 12 (2017) 1–4, <https://doi.org/10.1186/S11671-017-1978-Z>/FIGURES/3.
- [60] G. Su, X. Gao, T. Yan, D. Zhang, C. Cui, L. Du, Z. Liu, Y. Tang, J. Hu, Inter-critical tempering enables nanoscale austenite/ $\epsilon$ -martensite formation in low-C medium-Mn steel: a pathway to control mechanical properties, *Mater. Sci. Eng., A* 736 (2018) 417–430, <https://doi.org/10.1016/j.msea.2018.08.082>.
- [61] V.G. Gavriljuk, V.A. Sirosh, Y.N. Petrov, A.I. Tyshchenko, W. Theisen, A. Kortmann, Carbide precipitation during tempering of a tool steel subjected to deep cryogenic treatment, in: *Metal Mater Trans A Phys Metall Mater Sci*, Springer Boston, 2014, pp. 2453–2465, <https://doi.org/10.1007/s11661-014-2202-8>.
- [62] X. He, X. Lu, S. Wu, Q. Yong, J. Liang, J. Su, L. Zhou, J. Li, K. Zhao, M23C6 precipitation and Si segregation promoted by deep cryogenic treatment aggravating pitting corrosion of supermartensitic stainless steel, *J. Iron Steel Res. Int.* 28 (2021) 629–640, <https://doi.org/10.1007/s42243-020-00514-w>.
- [63] L. Tóth, Examination of the properties and structure of tool steel en . 1 . 2379 due to, *Different Heat Treatments 3* (2018) 1–7.
- [64] G. Su, X. Gao, M. Huo, H. Xie, L. Du, J. Xu, Z. Jiang, New insights into the corrosion behaviour of medium manganese steel exposed to a NaCl solution spray, *Construct. Build. Mater.* 261 (2020), 119908, <https://doi.org/10.1016/j.conbuildmat.2020.119908>.
- [65] M.A. Hafeez, Investigation on mechanical properties and immersion corrosion performance of 0.35%C–10.5%Mn steel processed by austenite reverted transformation (ART) annealing process, *Metallogr. Microstruct. Anal.* 9 (2020) 159–168, <https://doi.org/10.1007/S13632-020-00629-2>/FIGURES/9.
- [66] G. Su, C. Yu, H. Zheng, X. Gao, H. Xie, M. Huo, H. Wu, J. Xu, L. Du, Z. Jiang, The wet-dry cycling corrosion behavior of low-carbon medium manganese steel exposed to a 3.5% NaCl solution environment, *J. Mater. Eng. Perform.* 31 (2022) 7856–7869, <https://doi.org/10.1007/S11665-022-06819-Z>/TABLES/4.
- [67] H. Yang, X. Liu, X. Zhang, C. Wu, Y. Wang, X. Zhu, Y. Zhang, Z. Zhao, Effect of deposition of Al/AlN coating on medium-Mn steel on its corrosion resistance in 5 wt.% NaCl, *Int. J. Electrochem. Sci.* 17 (2022), 22123, <https://doi.org/10.20964/2022.12.02>.
- [68] G. Su, X. Gao, Comparison of medium manganese steel and Q345 steel on corrosion behavior in a 3.5 wt % NaCl solution, *Materials* 10 (2017) 938, <https://doi.org/10.3390/MA10080938>, 10 (2017) 938.
- [69] D. Zhang, X. Gao, G. Su, L. Du, Z. Liu, J. Hu, Corrosion behavior of low-C medium-Mn steel in simulated marine immersion and splash zone environment, *J. Mater. Eng. Perform.* 26 (2017) 2599–2607, <https://doi.org/10.1007/S11665-017-2723-6>/TABLES/2.
- [70] X. Yan, S. Kang, M. Xu, P. Li, Corrosion product film of a medium-Mn steel exposed to simulated marine splash zone environment, *Materials* 14 (2021), <https://doi.org/10.3390/MA14195652>.
- [71] G. Su, X. Gao, L. Du, D. Zhang, J. Hu, Z. Liu, Influence of Mn on the corrosion behaviour of medium manganese steels in a simulated seawater environment, *Int. J. Electrochem. Sci.* 11 (2016) 9447–9461, <https://doi.org/10.20964/2016.11.51>.
- [72] R. Feng, J. Beck, D. Hall, A. Buyuksagis, S. Lvov, M. Ziomek-Moroz, M. Doe Ziomek, Effects of CO<sub>2</sub> and H<sub>2</sub>S on corrosion of martensitic steels in NaCl at low temperature, in: *NACE Corrosion*, 2016 n.d., [https://www.researchgate.net/publication/301895534\\_Effects\\_of\\_CO2\\_and\\_H2S\\_on\\_Corrosion\\_of\\_Martensitic\\_Steels\\_in\\_NaCl\\_at\\_Low\\_Temperature](https://www.researchgate.net/publication/301895534_Effects_of_CO2_and_H2S_on_Corrosion_of_Martensitic_Steels_in_NaCl_at_Low_Temperature). (Accessed 8 February 2023).

- [73] F.H. Estupiñán López, C. Gaona Tiburcio, P. Zambrano-Robledo, J.A. Cabral, F. Almeraya Calderon, Electrochemical study of 17-4 and 17-7 PH stainless steels used in the aeronautical industry, in: Proceedings of the Symposium of Aeronautical and Aerospace Processes, Materials and Industrial Applications, 2018, pp. 63–71, [https://doi.org/10.1007/978-3-319-65611-3\\_6](https://doi.org/10.1007/978-3-319-65611-3_6).
- [74] A. Szewczyk-Nykiel, J. Kazior, Effect of aging temperature on corrosion behavior of sintered 17-4 PH stainless steel in dilute sulfuric acid solution, *J. Mater. Eng. Perform.* 26 (2017) 3450–3456, <https://doi.org/10.1007/S11665-017-2778-4/TABLES/4>.
- [75] Y. Liu, Q. Zhao, J. Zhao, Y. Huang, X. Cheng, L. Lu, Effect of pre-passivation on the corrosion behavior of PH13-8Mo stainless steel in industrial—marine atmospheric environment, *Front. Mater.* 6 (2019) 296, <https://doi.org/10.3389/FMATS.2019.00296/BIBTEX>.
- [76] 17-4 PH stainless steel – Progressive alloy steels unlimited (n.d.), <https://www.progressivealloy.com/17-4-ph-stainless-steel/>. (Accessed 8 February 2023).
- [77] PH 13-8 MO Data Sheet | Buy 1.4534 | S+D METALS - your stock and service expert for high-performance material as CP Titanium, Titanium alloys and special steels, n.d. <https://www.sd-metals.com/en/s-d-materials/special-stainless-steel/ph-13-8-mo-1-45354/>. (Accessed 8 February 2023).
- [78] M. Kang, Y.M. Kim, H.N. Han, C. Kim, Effects of phase evolution on mechanical properties of laser-welded ferritic Fe-Al-Mn-C steel, *Metals* 7 (2017) 523, <https://doi.org/10.3390/MET7120523>, 7 (2017) 523.
- [79] G. Luan, O. Volkova, J. Mola, Tensile deformation behavior of medium manganese steels with high carbon concentrations and austenitic microstructures, *Metals* 8 (2018) 902, <https://doi.org/10.3390/MET8110902>, 8 (2018) 902.
- [80] A. Grajcar, A. Kilarski, A. Kozłowska, Microstructure–property relationships in thermomechanically processed medium-Mn steels with high Al content, *Metals* 8 (2018) 929, <https://doi.org/10.3390/MET8110929>, 8 (2018) 929.
- [81] L.E. Umoru, A.A. Afonja, B. Ademodi, Corrosion study of AISI 304, AISI 321 and AISI 430 stainless steels in a tar sand digester, *J. Miner. Mater. Char. Eng.* 7 (2008) 291–299.
- [82] AHSS corrosion resistant coatings - AHSS guidelines, n.d. <https://ahssinsights.org/main-blog/ahss-corrosion-resistant-coatings/>. (Accessed 8 February 2023).
- [83] F. Li, H. Liu, W. Shi, R. Liu, L. Li, Hot dip galvanizing behavior of advanced high strength steel, *Mater. Corros.* 63 (2012) 396–400, <https://doi.org/10.1002/MACO.201005905>.
- [84] T. Allam, X. Guo, S. Sevsek, M. Lipí Nska-Chwalek, A. Hamada, E. Ahmed, W. Bleck, Development of a Cr-Ni-V-N medium manganese steel with balanced mechanical and corrosion properties, *Metals* 9 (2019) 705, <https://doi.org/10.3390/met9060705>.
- [85] K.D. Bauer, M. Todorova, K. Hingerl, J. Neugebauer, A first principles investigation of zinc induced embrittlement at grain boundaries in bcc iron, *Acta Mater.* 90 (2015) 69–76, <https://doi.org/10.1016/J.ACTAMAT.2015.02.018>.
- [86] Q. Lu, Q. Lai, Z. Chai, X. Wei, X. Xiong, H. Yi, M. Huang, W. Xu, J. Wang, Revolutionizing car body manufacturing using a unified steel metallurgy concept, *Sci. Adv.* 7 (2021) 176, [https://doi.org/10.1126/SCIADV.ABK0176/SUPPL\\_FILE/SCIADV.ABK0176\\_SM.V1.PDF](https://doi.org/10.1126/SCIADV.ABK0176/SUPPL_FILE/SCIADV.ABK0176_SM.V1.PDF).
- [87] Understanding cryogenic freezing tunnels | 2019-05-20 | process cooling (n.d.), <https://www.process-cooling.com/articles/89713-understanding-cryogenic-freezing-tunnels>. (Accessed 8 February 2023).
- [88] M. Mia, M.A. Rahman, M.K. Gupta, N. Sharma, M. Danish, C. Prakash, Advanced cooling-lubrication technologies in metal machining, *Machin. Tribol.* (2022) 67–92, <https://doi.org/10.1016/B978-0-12-819889-6.00010-1>. Processes, Surfaces, Coolants, and Modeling.
- [89] Y. Yildiz, M. Nalbant, A review of cryogenic cooling in machining processes, *Int. J. Mach. Tool Manufact.* 48 (2008) 947–964, <https://doi.org/10.1016/J.IJMACHTOOLS.2008.01.008>.
- [90] A. Kwiatkowski da Silva, I.R. Souza Filho, W. Lu, K.D. Zilnyk, M.F. Hupalo, L. M. Alves, D. Ponge, B. Gault, D. Raabe, A sustainable ultra-high strength Fe18Mn3Ti maraging steel through controlled solute segregation and  $\alpha$ -Mn nanoprecipitation, *Nat. Commun.* 13 (2022) 1–8, <https://doi.org/10.1038/s41467-022-30019-x>, 1. 13 (2022).